

## Monte Carlo simulations of nanosecond electromagnetic pulse interaction with field-aligned ionospheric plasma density irregularities

M. Kirillin, E. Sergeeva, D. Kurakina, I. Zudin, and M. Gushchin

A.V. Gaponov-Grekhov Institute of Applied Physics of Russian Academy of Sciences,  
46 Ulyanov Street, Nizhny Novgorod 603950, Russia

Corresponding author: Mikhail Kirillin ([kirillin@ipfran.ru](mailto:kirillin@ipfran.ru))

## **Key Points:**

- Monte Carlo model of nanosecond electromagnetic pulse propagation in ionospheric plasma with field-aligned density depletions is developed
  - Frequency dispersion competes with pronounced pathlength dispersion for scattered waves at low frequencies.
  - The effects of density depletions on electromagnetic pulse properties seem weak even for strong plasma density depletions of up to 50%.

1

17    **Abstract**

18    We propose an approach to simulate ultra-wideband (UWB) electromagnetic pulse (EMP)  
 19    propagation in ionosphere with magnetic field-aligned irregularities of plasma density based on  
 20    Monte Carlo technique. This approach considers propagation of a nanosecond EMP by ray  
 21    trajectories in frequency domain, which allows one to analyze the role of scattering effects for  
 22    lower and higher harmonics of the pulse. Parameters of the irregularities used in the  
 23    simulations are chosen close to those of artificial ionospheric turbulence (AIT) density striations  
 24    stimulated by high-frequency (HF) heating facilities. The employed technique provides a  
 25    possibility to compare the effects of dispersion and scattering on a waveform of bipolar  
 26    nanosecond EMP for various parameters of ionospheric plasma and its disturbances. In the  
 27    presence of 10-meter scale, 10-percent level density striations, we show that lower frequencies  
 28    are most responsible for the EMP waveform transformation due to the plasma dispersion, and  
 29    are scattered away from the initial propagation direction, while higher frequencies experience  
 30    minor dispersion and are less scattered. The influence of AIT-type striations on the  
 31    straightforward EMP delay and its broadening in time domain is analyzed compared to the EMP  
 32    propagation in uniform plasma. Preliminary, the effects of AIT-type striations on EMP  
 33    characteristics seem to be weak in the main part of its frequency spectrum, even for strong  
 34    (non-realistic) plasma density depletions of up to 50%.

35

36    **1 Introduction**

37       Ultrawideband (UWB) electromagnetic pulses (EMPs) are signals with duration from  
 38    tens of picoseconds to several nanoseconds. The frequency spectrum of such signals is very  
 39    broad, from about 100 MHz to 10 GHz, since EMPs are as short as one cycle of oscillation of the  
 40    electromagnetic field. The development of UWB technology in recent decades (Agee et al.,  
 41    1998; Baum, 1992; Nekoogar, 2011) has led to discussion of the possibilities of UWB EMP use  
 42    for sounding the ionosphere and building trans-ionospheric radio communication channels  
 43    (see, for example, (Soldatov & Terekhin, 2016)). Recently, first experiment of trans-ionospheric  
 44    propagation of a nanosecond EMP with its reception onboard a satellite was reported (Zhang et  
 45    al., 2024).

46       In this regard, questions inevitably arise about the effect of ionospheric plasma on the  
 47    waveform and frequency spectrum of UWB EMP, primarily the effects of dispersion and  
 48    scattering on natural and artificial electron density irregularities along the EMP propagation  
 49    path. The role of linear dispersion and linear absorption leading to the spreading of the UWB  
 50    EMP and a decrease in its amplitude has been extensively studied (see (Arnush, 1975;  
 51    Cartwright & Oughstun, 2009; Dvorak, et al, 1997) and references therein), as well as nonlinear  
 52    effects for high-power EMPs (Golubev, et al, 2000). Laboratory simulations of UWB EMP  
 53    propagation in ionosphere are also being developed under the support of analytical and  
 54    numerical models (Es'kin, et al, 2023; Goykhman et al., 2022; Zudin et al., 2024). However, the  
 55    effects of ionospheric irregularities on the propagation of UWB EMPs have not been explicitly  
 56    studied yet, to our knowledge.

57        Generally, the effect of ionospheric irregularities on the propagation of very-high (VHF,  
 58 30 – 300 MHz), ultra-high (UHF, 300 MHz – 3 GHz), and super-high frequencies (SHF, 3 – 30  
 59 GHz) that overlap the UWB EMPs' frequency spectrum has been actively studied since the  
 60 1970s (Perkins, 1975). In recent years, interest in this problem is driven first of all by ensuring  
 61 the high accuracy of Global Navigation Satellite Systems (GNSS) that use L-band transmission  
 62 channels (see (Aol et al, 2020; Hong et al., 2020; Mrak et al, 2023; Wernik et al, 2003) and  
 63 references therein). To date, models of diffraction and scattering on natural ionospheric  
 64 irregularities with sizes from several kilometers to several meters have been developed that  
 65 allow one to estimate the amplitude and phase scintillations of monochromatic or narrowband  
 66 signals (Carrano et al, 2011; Deshpande et al, 2014; Galiègue et al 2017). These models,  
 67 however, cannot be explicitly applied to analyze the waveforms of UWB EMPs propagating in  
 68 disturbed ionosphere.

69        Artificial ionospheric irregularities (Alls) are a manifestation of artificial ionospheric  
 70 turbulence (AIT) which develops in ionosphere exposed to powerful radio waves (see (Streltsov  
 71 et al., 2018) and references therein). Generation of Alls and their effect on the propagation of  
 72 VHF waves were discovered in early experiments on ionosphere modification (Fialer, 1974).  
 73 Ground-based HF ionosphere heating facilities located at different geographic latitudes (SURA,  
 74 Russia; HAARP, USA; EISCAT-Heating, Norway) (Streltsov et al., 2018) are capable of generating  
 75 the Alls.

76        In scattering of high-frequency waves, the irregularities with scales from meters (and  
 77 even decimeters) to kilometers provide dominating impact. Properties of such Alls were studied  
 78 in sufficient detail from radar scattering after plasma modification by heating facilities, as well  
 79 as from the characteristics of artificial radio emission from ionosphere (Dhillon & Robinson,  
 80 2005; L. Erkhirimov et al, 1988; L. M. Erkhirimov & Mityakov, 1989; Franz et al, 1999; Frolov et  
 81 al, 1997; Grach et al, 2016). Direct measurements of Alls are complicated, however they were  
 82 performed in rocket experiment (Kelley et al., 1995). A simplified model of All system can be  
 83 represented as multiple plasma density depletions up to 10-20% from the background (or  
 84 "striations") oriented parallel to the geomagnetic field, (Franz et al., 1999; Kelley et al., 1995).  
 85 Owing to the pronounced anisotropic mobility of electrons and ions in the geomagnetic field,  
 86 Alls have nearly cylindrical shape. Axial All scale  $l_{\parallel}$  is limited by the thickness of the turbulence  
 87 area and can be as large as several tens of km. Transverse scale of the irregularities  $l_{\perp}$  can be  
 88 about 10 m or even less. Aspect ratio of irregularities  $l_{\parallel}/l_{\perp}$  can be of the order of the ratio of  
 89 frequency of electron collisions with neutral particles to electron gyrofrequency, which  
 90 amounts  $10^{-4}$  in ionospheric F-layer (Robinson, 2002).

91        Our interest in the effect of Alls on the propagation of EMPs in the GHz frequency range  
 92 is because such irregularities can be excited under controlled conditions and be quite small-  
 93 scaled, i.e. of the order of 10 m or less causing considerable scattering of short (meter and  
 94 decimeter) waves. Therefore, the developed models of UWB EMP scattering on ionospheric  
 95 irregularities can in future be verified in active experiments with heating facilities. To date, All-  
 96 caused scintillation of L-band signals has been observed using HAARP (Mahmoudian et al.,  
 97 2018) and EISCAT (Sato et al, 2021) heaters. Moreover, the possibility of generating Alls of very  
 98 small transverse scales of the order of 10 cm, or so-called "super small-scale" (SSS) irregularities  
 99 in the heating experiments is being discussed (Milikh et al, 2008). If density variations in SSS

100 irregularities reach 20-30% (Najmi et al., 2014), such Alls can in principle lead to strong  
101 scattering of GHz signals including UWB EMPs.

102 The frequencies of sub GHz and GHz waves significantly (by several orders of  
103 magnitude) exceed the plasma frequency of the F-layer which is typically below 10 MHz, and  
104 electron collision frequencies (Soldatov & Terekhin, 2016). This leads to a number of  
105 assumptions in a model of UWB EMP interaction with ionospheric irregularities: (1)  
106 approximation of collisionless plasma can be used; (2) the influence of geomagnetic field on the  
107 EMP dispersion can be neglected. Thus, plasma acts as a medium that is transparent to  
108 radiation and does not absorb electromagnetic energy, with an isotropic dielectric constant and  
109 a refractive index close to unity. The irregularities manifest themselves as refractive index  
110 variations (Hunsucker & Hargreaves, 2007), while scattering of GHz waves is determined by the  
111 geometry of irregularities exclusively, i.e. their depth and statistics. However, the three-  
112 dimensional geometry of striations turns out to be quite complex, which complicates  
113 achievement of analytical solutions.

114 To simulate the propagation of GHz waves in ionosphere in the presence of Alls  
115 numerically, a parabolic wave equation (PWE) is used in combination with a series of phase  
116 screens (PSs) that carry information about random distribution of refractive index along the  
117 propagation path. Note that similar numerical approach is widely used to assess the effects of  
118 atmospheric turbulence on electromagnetic wave propagation (Deshpande et al., 2014; Knepp,  
119 2005). Given the limited performance of machine calculations in ionospheric research, two-  
120 dimensional PWE in combination with multiple one-dimensional PSs was previously used to  
121 estimate ionospheric scintillations (Carrano et al., 2011). Due to low dimensionality of the  
122 method, the interpretation and applicability of the results was limited. To represent a realistic  
123 geometry in the case when the EMP propagation path through the ionosphere is several  
124 hundred kilometers and the Alls are obviously three-dimensional, it was proposed to use a  
125 three-dimensional PWE in combination with a series of two-dimensional PSs (Galiègue et al.,  
126 2017), which made it possible to refine the solution at the cost of significant increase of the  
127 calculation time.

128 A good alternative are statistical numerical methods like Monte Carlo (MC) technique  
129 which are actively employed in the wave propagation and energy transport problems. Monte  
130 Carlo method is based on repeated simulation of random ray trajectories and subsequent  
131 statistical processing and analysis of the results obtained. This method is used in various fields  
132 of atmospheric (Marchuk et al., 2013) and ionospheric (Kim, Yoon, Lee, Pullen, & Weed, 2017;  
133 Mountcastle & Martin, 2002; Schlegel, 1973) physics, optics of ocean (Leathers et al, 2004; A.  
134 Luchinin & Kirillin, 2017) and biological tissues (Kirillin et al, 2014; Yan & Fang, 2020). When  
135 applied to the problems of propagation of electromagnetic waves in randomly inhomogeneous  
136 media, the Monte Carlo method allows one to estimate the characteristics of signal amplitudes  
137 and phases after their scattering and absorption in a volume with random dielectric  
138 irregularities. Random medium can be defined by a set of irregularities with known sizes and  
139 refractive index variations, as well as by spatially distributed statistical characteristics of  
140 scattering and absorption. Flexibility in setting the medium properties provides an advantage  
141 for MC technique compared to analytical and semi-analytical modeling that requires  
142 information about the spectral correlation characteristics of the medium which is often

143 available only empirically. Another important point is that MC technique is successfully used to  
 144 solve problems of propagation of ultrashort (similarly, UWB) pulses in randomly  
 145 inhomogeneous media (A. G. Luchinin et al, 2019; A. G. Luchinin & Kirillin, 2021; A. G. Luchinin  
 146 et al, 2024; Sergeeva, Kirillin, & Priezzhev, 2006).

147 The aim of the current paper is to present a methodology based on the Monte Carlo  
 148 technique for modeling the propagation of a nanosecond EMP in the ionospheric plasma  
 149 allowing to account for both the dispersion of the EMP in plasma and the effects associated  
 150 with scattering on small-scaled field-aligned ionospheric plasma irregularities.

151

## 152 **2 Model description**

### 153        2.1     UWB EMP and ionospheric plasma model

154 Let us consider a plane linearly polarized electromagnetic wave with an electric field  
 155  $E_0(\tau = t - z/c)$  which propagates downwards along vertical direction coinciding the z axis  
 156 through a plasma layer of total thickness  $Z_{layer}$ , where c is the speed of light in vacuum. We  
 157 assume the nanosecond EMP of duration  $\tau_0$  is generated at the top of the layer in the plane  $z =$   
 158 0 and has a bipolar shape (Soldatov & Terekhin, 2016):

$$159 \quad E_0(\tau) = H(\eta)H(1 - \eta)\eta(\eta - 0.5)(\eta - 1) \quad (1)$$

160 where  $\eta = \tau/\tau_0$  and  $H(\eta)$  is the Heaviside step function. In frequency domain, the  
 161 shape of the initial EMP is characterized by spectrum  $\tilde{E}_0(f)$ :

$$162 \quad \tilde{E}_0(f) = \int_{-\infty}^{\infty} E_0(\tau) \exp(-j2\pi f\tau) d\tau. \quad (2)$$

163 Complex amplitude  $\tilde{E}(f, z)$  of the signal harmonic the with the frequency f depends on  
 164 the pathlength z in uniform plasma as follows:

$$165 \quad \tilde{E}(f, z) = \tilde{E}_0(f) \exp\left(j\frac{z}{c}(1 - n(f))\right), \quad (3)$$

166 where

$$167 \quad n(f) = \sqrt{1 - f_p^2/f^2} \quad (4)$$

168 is the refractive index in plasma with plasma frequency  $f_p$ . We suppose the frequency  
 169 spectrum of a nanosecond EMP propagating in ionosphere belongs to the range from tens MHz  
 170 to several GHz. For frequencies exceeding the plasma frequency of the F-layer, we neglect the  
 171 effects of collisions and typical features of wave propagation in the ionosphere located in the  
 172 geomagnetic field such as the splitting of the dielectric constant for O-mode and X-mode,  
 173 reflection of waves and their thermal dissipation. The main effect of the interaction consists  
 174 here in linear scattering of frequency harmonics as they pass through the refractive index  
 175 irregularities associated with Alls.

176 Figure 1 shows the evolution of EMP shape after its propagation in uniform plasma layer  
 177 with thickness of  $Z_{layer} = 30$  km and plasma frequency  $f_p = 5$  MHz calculated using Eq. (3), as  
 178 well as the its spectrum. Due to dispersion, the shape of UWB EMP undergoes significant

179 changes including shape distortion and considerable center of mass displacement. Pulse center  
 180 of mass delay  $\langle\tau\rangle$  and pulse width  $\delta\tau$  can be estimated numerically as:

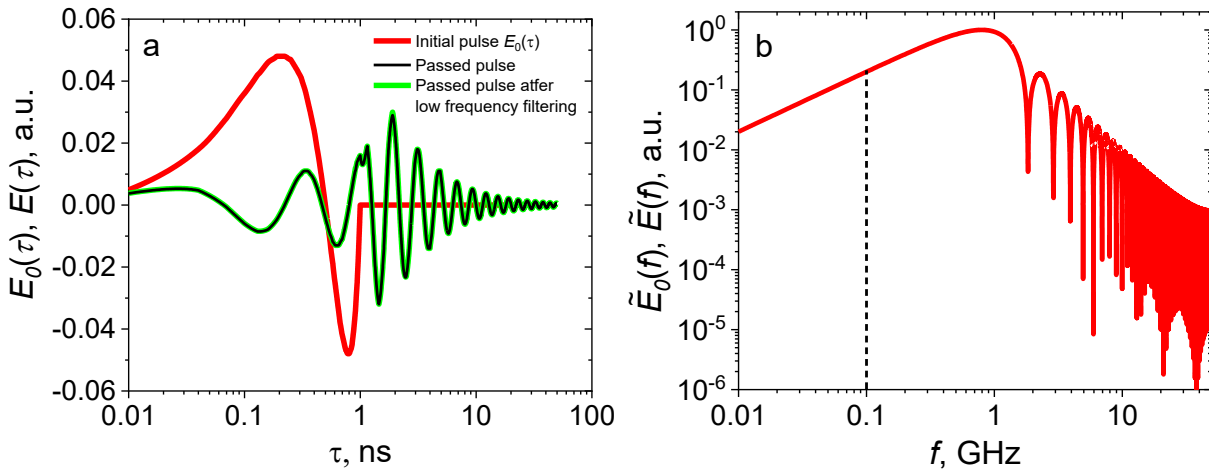
$$181 \quad \langle\tau\rangle = \int_0^{\infty} E^2(\tau) \tau dt / \int_0^{\infty} E^2(\tau) dt, \quad (5)$$

$$182 \quad \delta\tau = \sqrt{\int_0^{\infty} E^2(\tau) \tau^2 dt / \int_0^{\infty} E^2(\tau) dt - \langle\tau\rangle^2}. \quad (6)$$

183 For propagation in free space the pulse characteristics are  $\langle\tau\rangle = 0.5\tau_0$  and  
 184  $\delta\tau \approx 0.29\tau_0$ . Note that even in the absence of Alls, dispersion along the path leads to an  
 185 increase of the pulse delay and width by more than 10 times.

186 In the presence of Alls, refractive index irregularities lead to the EMP scattering, and,  
 187 consequently, to the additional modification of its shape which will be analyzed further within  
 188 the framework of Monte Carlo simulation.

189



190  
 191 **Figure 1.** Shape of initial bipolar UWB EMP with duration of  $\tau_0 = 1$  ns calculated by Eq.(1) and its  
 192 profile after propagation within a uniform plasma layer of the thickness of 30 km with plasma  
 193 frequency  $f_p = 5$  MHz as well as the passed pulse profile after filtering the frequencies below 100  
 194 MHz (a); amplitudes of frequency spectrum of initial pulse (b).

195 2.2 Monte Carlo technique for modeling the UWB EMP propagation in ionospheric  
 196 plasma with irregularities

197 Among methods that analyze propagation of electromagnetic radiation in a random  
 198 medium, Monte Carlo technique implements the principle of wave-particle duality. A wave is  
 199 presented as a bundle of rays where each ray defines propagation of a small section of the  
 200 wave front. Random trajectory of each ray is simulated as a set of adjacent piecewise linear  
 201 sections. The nodes at the connections of these sections are the points of the ray interaction

202 with the scatterers. To consider the wave phenomena, each ray is assigned with the wave  
 203 attributes, such as amplitude and phase, which vary depending on the particular ray trajectory  
 204 in the medium.

205           2.2.1 Frequency domain approach

206       One of the advantages of Monte Carlo method in the problem of UWB EMP propagation  
 207 in ionospheric plasma is its ability to evaluate the effect of Alls in a certain plasma layer on the  
 208 scattering of the ray. In radiation transfer problems, Monte Carlo method can be implemented  
 209 using one of the two most general schemes: (1) a classical scheme with random arrangement of  
 210 scatterers when all scattering events are considered independent, and the position of each  
 211 scatterer is determined at each step based on a priori given scattering and absorption parameters  
 212 of the medium, and (2) a so-called "fixed particle Monte Carlo" (Xiong et al., 2005) in which the  
 213 positions of the scatterers in the medium are defined in advance.

214       In the first scheme, the result of calculation is the average over various possible  
 215 ensembles of scatterers, while the second scheme makes it possible to account for the  
 216 characteristics of radiation propagation within the mean free path in a particular ensemble of  
 217 scatterers. In this study, we used the first classical approach which allows one to obtain a result  
 218 averaged over various ensembles leading to a more general solution compared to a particular  
 219 solution obtained within the second approach.

220       Let us consider the implementation of Monte Carlo algorithm for modeling the ray  
 221 trajectory of  $k$ -th harmonic  $f_k$  from the EMP spectrum defined by Eq. (2) in a layer of ionospheric  
 222 plasma in the presence of Alls. Geomagnetic field aligned cylindrical striations (see Fig.2) are  
 223 considered as a statistical ensemble of scatterers. For simplicity all irregularities are assumed to  
 224 be of the same size but with a varying in-between distance. The input parameters for modeling  
 225 are the harmonic frequency  $f_k$ , plasma frequency  $f_p$  corresponding to the average electron  
 226 density value in the plasma layer, radius  $r$  of a single irregularity, mean ray free path (RFP)  $\langle l \rangle$   
 227 between two adjacent irregularities, depth  $\delta$  of relative electron density depletions within the  
 228 irregularity, and thickness  $Z_{layer}$  of plasma layer containing striations. The properties of EMP  
 229 after passing the plasma layer with striations are analyzed at the layer lower boundary  
 230  $z = Z_{layer}$ , which is called "detector plane". Detection area is divided into segments with center  
 231 position  $(x_a, y_b)$  and size  $\Delta x \times \Delta y$  where  $\Delta x$  and  $\Delta y$  are dimensions along the corresponding axes.

232       Calculation is based on consequent tracking of  $N$  rays which travel from the origin through  
 233 the plasma layer. Let  $i$ -th ray ( $i = 1\dots N$ ) corresponding to the harmonic with frequency  $f_k$  be  
 234 assigned with a local scalar field:

235           
$$E_{i,k}(x, y, z, \tau) = E_{0,k} \cos(2\pi f_k(\tau + z/c) + \varphi_{0,k} - \phi_{i,k}), \quad (7)$$

236       where  $E_{0,k}$  and  $\varphi_{0,k}$  are, respectively, the field amplitude and initial phase of the harmonic in the  
 237 plane  $z = 0$ , and  $\phi_{i,k} = \phi_{i,k}(x, y, z)$  is the phase shift along the pathway in dependence on  
 238 Cartesian coordinates. Local propagation direction is defined by three direction cosines  
 239 ( $\gamma_x, \gamma_y, \gamma_z$ ). Random RFP between the two consecutive scattering events is calculated in  
 240 accordance with semi-empirical concept of single scattering described by the Bouger-Lambert-

241 Beer's law. It defines the average intensity  $I(z)$  of the non-scattered plane wave after passing  
 242 the distance  $z$  in the scattering and non-absorbing medium as:

$$243 \quad I(z) = I_0 \exp(-\mu_s z), \quad (8)$$

244 where  $I_0$  is the initial intensity and  $\mu_s$  is the scattering coefficient of the medium which is the  
 245 inverse to the mean free path in the medium:  $\mu_s = 1/\langle l \rangle$ . In this connection, current RFP is  
 246 calculated as follows:

$$247 \quad l = -\ln(\xi)/\langle l \rangle, \quad (9)$$

248 where  $\xi$  is a random magnitude uniformly distributed uniformly in the range (0,1].

249 Interaction of the ray with each irregularity is considered within the framework of  
 250 geometric optics approach under the assumption that the transverse size of the irregularity  
 251 significantly exceeds the wavelength for all harmonics of a nanosecond EMP, which limits the  
 252 lowest spectrum frequency. One iteration of a ray tracing cycle includes searching the  
 253 intersection point of the ray trajectory with a cylinder, calculating reflection coefficient  $R_{ref}$  of  
 254 the ray by the cylinder surface in accordance with the Fresnel law. Occurrence of reflection is  
 255 defined by the condition:

$$256 \quad \eta < R_{ref}, \quad (10)$$

257 where  $\eta$  is a random magnitude uniformly distributed in the range (0,1]. If condition (10) is met,  
 258 the ray direction changes in accordance with the reflection law, and a new RFP in the external  
 259 medium is generated according to Eq. (9). If condition (10) is violated, refraction of the ray occurs.  
 260 The ray changes its direction according to the Fresnel law and propagates through the irregularity  
 261 to its far boundary, where the reflection test using condition (10) is performed again. Simulation  
 262 of the ray propagation inside the irregularity is performed until a refraction event occurs at the  
 263 cylinder-plasma boundary and the ray exits into the surrounding plasma. In this case, a new  
 264 iteration begins by evaluation of the free path using Eq. (9). Iterations are repeated until the ray  
 265 exits the boundaries of the medium or reaches the detector plane  $z = Z_{layer}$  which coincides  
 266 with the lower boundary of the layer with irregularities. Output coordinates  $(x_i^{ex}, y_i^{ex})$  of the i-th  
 267 ray in the detection plane are recorded together with the total phase shift  $\phi_{i,k}^{ex}$ :

$$268 \quad \phi_{i,k}^{ex} = 2\pi f_k (n(f_k) L_{p,i} + n_{str}(f_k) L_{str,i}) / c, \quad (11)$$

269 where  $L_{p,i}$  is the total ray path in surrounding plasma,  $L_{str,i}$  is the total ray path inside  
 270 irregularities, and  $n_{str}$  is the refractive index inside the irregularity:

$$271 \quad n_{str}(f) = \sqrt{1 - f_p^2(1 - \delta)/f^2}. \quad (12)$$

272 At the final stage, averaging of field oscillations  $E_{i,k}(x^{ex}, y^{ex}, \tau) = \tilde{E}_{0,k}(f) \cos(2\pi f_k(\tau +$   
 273  $Z_{layer}/c) + \varphi_{0,k} - \phi_{i,k}^{ex})$  of all rays reaching the detector plane  $z = Z_{layer}$  within the segment  
 274  $(x_a, y_b)$  is performed:

$$275 \quad E_k^{ray}(x_a, y_b, \tau) = \sum_{i|x_a < x_i^{ex} < x_a + \Delta x, y_b < y_i^{ex} < y_b + \Delta y} E_{i,k}(x_i^{ex}, y_i^{ex}, Z_{layer}, \tau) / N. \quad (13)$$

276 It is assumed in Eq. (13) that the output direction of the ray does not change significantly with  
 277 respect to the initial direction.

## 278        2.2.2 Frequency scattering map construction

279        To analyze the structure of the EMP in space and time, it is convenient to present the  
 280        pulse by a discrete Fourier spectrum with a set of harmonics  $f_k = k/T$  ( $k = 1 \dots N_k$ ):

$$281 \quad \tilde{E}_{0,k} = \frac{1}{T} \int_0^T E_0(\tau) \exp(-j2\pi f_k \tau) d\tau, \quad (14)$$

282        where T is the pulse record time. Previously described Monte Carlo simulation of ray propagation  
 283        can be then performed for each harmonic  $f_k$  followed by summation for all harmonics within the  
 284        detector segment  $(x_a, y_b)$ :

$$285 \quad E^{pulse}(x_a, y_b, \tau) =$$

$$286 \quad = \sum_k E_k^{ray}(x_a, y_b, \tau) = \sum_k \sum_{i|x_a < x_i^{\text{ex}} < x_a + \Delta x, y_b < y_i^{\text{ex}} < y_b + \Delta y} E_{0,i}^k \cos(2\pi f_k(\tau + Z_{layer}/c) + \varphi_{0,k} - \phi_{i,k}^{\text{ex}}). \quad (15)$$

287        For better visual representation of both effects of scattering and dispersion on the EMP  
 288        propagation we propose to construct “frequency scattering maps” similar to construction of a  
 289        point spread function. These maps illustrate the deviations of particular frequency harmonics  
 290        from straight forward propagation due to scattering, and their arrival to a particular detector  
 291        segment  $(x_a, y_b)$ . Such maps can provide a complete picture of the scattering role in ray deflecting  
 292        from the straight forward propagation. We constructed the 2D map of minimal  $D_f^{\min}$  and  
 293        maximal  $D_f^{\max}$  nonzero frequencies of the pulse discrete spectrum  $\tilde{E}$ :

$$294 \quad D_f^{\min}(x_a, y_b) = \min(f_k | \tilde{E}(x_a, y_b, f_k) > 0) \quad (16)$$

$$295 \quad D_f^{\max}(x_a, y_b) = \max(f_k | \tilde{E}(x_a, y_b, f_k) > 0) \quad (17)$$

296        To our knowledge, it is the first example of this approach in the analysis of spatial-spectral  
 297        structure of EMPs in a plasma medium.

## 298        2.2.3 Simulation of plane wave

299        When the source is located at a fairly large distance from the ionospheric layer (significantly  
 300        exceeding its thickness), the problem can be considered in the plane wave approximation. It  
 301        means that electric field is transversely uniform in the plane of the layer boundary and the  
 302        solution obtained for a single ray can be averaged over the detection plane. The solution for a  
 303        plane wave can be obtained as follows:

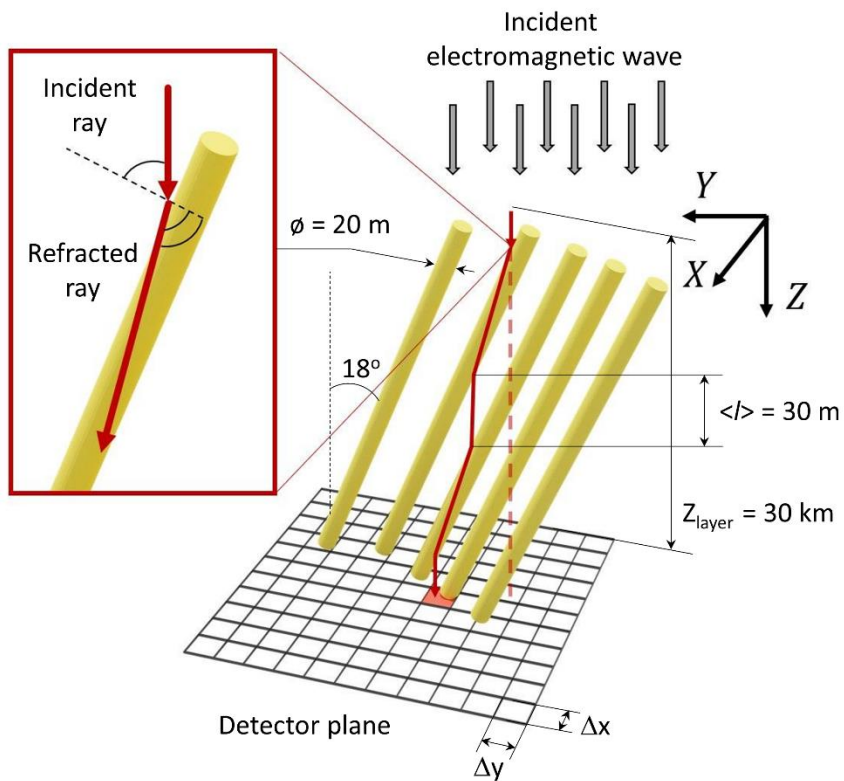
$$304 \quad E^{planar}(\tau) = \sum_{a,b} E^{pulse}(x_a, y_b, \tau) =$$

$$305 \quad = \sum_{a,b} \sum_k \sum_{i|x_a < x_i^{\text{ex}} < x_a + \Delta x, y_b < y_i^{\text{ex}} < y_b + \Delta y} E_{0,i}^k \cos(2\pi f_k(\tau + Z_{layer}/c) + \varphi_{0,k} - \phi_{i,k}^{\text{ex}}). \quad (18)$$

306        In the case of modeling a spherical wave, the effect of the shape of the spherical front can be  
 307        accounted by modeling a set of rays with individual initial directions, initial phase shift and  
 308        coordinates of the entry point into the layer based on an a priori given position of the source.  
 309        Modeling with such initial parameters is carried out separately for each harmonic.

## 310        2.3     Problem statement

311        In this study, we considered propagation of an EMP in a layer of ionospheric plasma of  
 312        thickness of  $Z_{layer} = 30$  km containing cylindrical irregularities with radius of  $r = 10$  m oriented  
 313        at an angle of  $\alpha = 18^\circ$  relative to vertical direction which mimic striations formed under mid-  
 314        latitude ionospheric heating conditions (Kelley et al., 1995). Average RFP between the  
 315        irregularities was chosen as  $\langle l \rangle = 30$  m. Relative depth of electron density depletions within  
 316        striations varied in the range of  $\delta = 5\% - 50\%$ . The largest values of  $\delta$  are hardly realistic, and  
 317        used in simulations in demonstrative purposes only. Two values of electron density in  
 318        unperturbed plasma were considered corresponding to plasma frequencies  $f_p = 5$  MHz and 10  
 319        MHz. The pulse duration  $\tau_p$  was assumed to be equal to 1 ns, its initial profile in the plane  $z = 0$   
 320        was given by Eq.(1). Typical trajectory of a ray propagating in the layer with the cylindrical  
 321        irregularities is shown in Fig. 2. The number of random ray trajectories used in the simulations  
 322        for individual harmonics varied in the range of  $N = 10^5 - 10^6$ . Detector plane had the size of 4000  
 323        m in X direction and 160 m in Y direction, while the size of segments  $\Delta x$  and  $\Delta y$  are 1 m on  
 324        default, and could be specified differently in separate cases.



325

326        **Figure. 2.** Schematic of the model: typical ray trajectory when scattering on ionospheric  
 327        irregularities.

328 **3 Simulation results**329       **3.1 Frequency spectrum of a nanosecond pulse in Monte Carlo simulations**

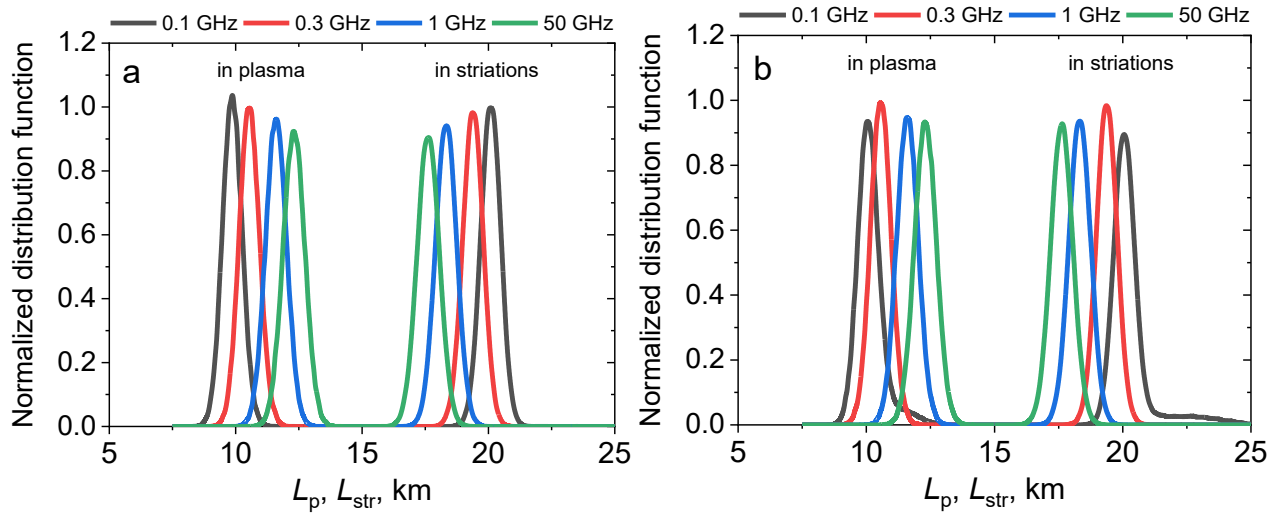
330       First, we have to define the number  $N_k$  of discrete Fourier spectrum harmonics  
 331 employed in Monte Carlo simulations of UWB EMP propagating in plasma with striations  
 332 according to Eq.(14). The shape of the initial 1-ns pulse given by Eq. (1) is shown in Fig.1 (a)  
 333 while analytically calculated harmonic spectrum of the initial pulse and the pulse passing a layer  
 334 of uniform plasma with plasma frequency  $f_p = 5$  MHz are shown in Fig.1(b). Lower frequency  
 335 limit of 10 MHz is related to the pulse record time of 100 ns, while upper frequency limit of 50  
 336 GHz is caused by temporal resolution of the incident pulse which was taken as  $10^{-2}$  ns. Total  
 337 number of counts used in analytical calculation is  $N_{\text{counts}} = 10^4$  yielding  $N_k = N_{\text{counts}}/2 = 5 \cdot 10^3$   
 338 harmonics required to compose the pulse.

339       In Monte Carlo modeling of the ray propagation in plasma with striations, several  
 340 assumptions are made which put certain restrictions on the harmonic spectrum of the pulse.  
 341 First, the transverse scale of striations is assumed large compared to the particular harmonic  
 342 wavelength so that ray optics can be employed. In the case  $r = 10$  m this condition is met for  
 343 frequencies not less than 100 MHz which means the first 10 harmonics in the range of 10-100  
 344 MHz should be withdrawn from the EMP spectrum. Fig.1(a) demonstrates the effect of low-  
 345 frequency filtering on the distortion of the passed pulse shape. The effect is rather minor and it  
 346 is almost negligible in the main body of the pulse in the range of 1-10 ns since the relative loss  
 347 of energy due to the withdrawn harmonics is below 0.2%. Another restriction comes from large  
 348 number of harmonics needed to be simulated for correct reconstruction of a scattered pulse  
 349 shape, which leads to intensive Monte Carlo modeling. In sub-GHz and GHz range the effect of  
 350 the ray refraction is mostly pronounced for lower harmonics while higher harmonics experience  
 351 less refraction. The question is in defining the domain of higher harmonics for which phase  
 352 delay can be evaluated analytically avoiding time-consuming Monte Carlo tracing.

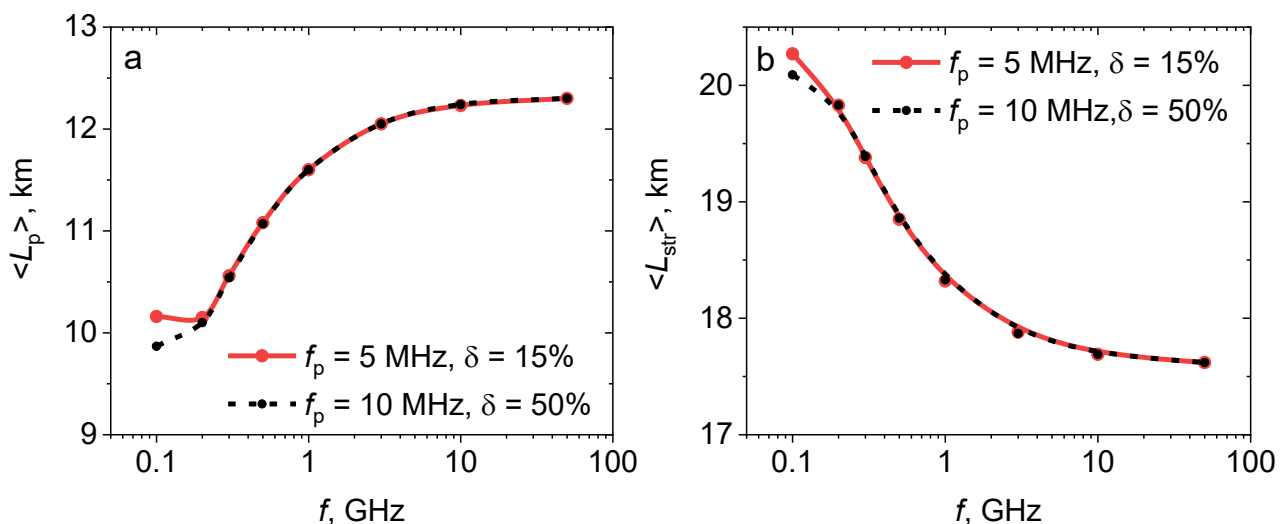
353       **3.2 Ray trajectories for different frequency harmonics**

354       We considered tracing a single pulsed ray incident on a 30-km-thick layer of plasma in  
 355 the origin ( $x = 0, y = 0, z = 0$ ) and directed along Z axis. We simulated the ray propagation in the  
 356 plasma layer with plasma frequency  $f_p = 5$  MHz containing density irregularities with  $\delta = 15\%$   
 357 which corresponds to some observations (Kelley et al., 1995), as well as the layer with plasma  
 358 frequency  $f_p = 10$  MHz with the irregularities with  $\delta = 50\%$  which is beyond natural conditions  
 359 and is presented as a limiting case. Fig. 3 demonstrates normalized statistical distribution of ray  
 360 pathlengths in plasma ( $L_p$ ) and in striations ( $L_{\text{str}}$ ) registered in the whole detector plane  
 361  $z = Z_{\text{layer}}$  for four individual EPM harmonics with frequencies of 0.1 GHz, 0.3 GHz, 1 GHz and  
 362 50 GHz. In the case of small  $\delta$  (Fig. 3a) all distributions are Gaussian-shaped with peak position  
 363 and width depending on the harmonic frequency. Lower harmonics are characterized by  
 364 smaller pathlengths in plasma and larger pathlengths within irregularities, as well as by  
 365 narrower width of the distribution. In the case of large  $f_p$  and  $\delta$  (Fig. 3b) the pathlength  
 366 distribution function is asymmetric for lowest harmonics with noticeable contribution of large  
 367 pathlengths both in striations and in the surrounding plasma which describes wandering of the

368 ray due to multiple refractions. Dependence of average pathlengths  $\langle L_p \rangle$  and  $\langle L_{str} \rangle$  on the  
 369 frequency for both cases of  $(f_p, \delta)$  is plotted in Fig. 4 for eight harmonics within the range 0.1 –  
 370 50 GHz. Average pathlength increases in plasma with the harmonic frequency (Fig. 4a) while it  
 371 decreases within striations (Fig. 4b) thus showing the lowering effect of refraction in higher  
 372 harmonics. The curves  $\langle L_p \rangle$  and  $\langle L_{str} \rangle$  are almost identical for both cases of  $(f_p, \delta)$  except for  
 373 the region of smallest frequencies where the effect of large-path tail in the distribution for  $f_p =$   
 374 10 MHz and  $\delta = 50\%$  is evident. Asymptotic average pathlength at high frequencies is almost  
 375 the same for weak and strong electron density depletions and amounts about  $\langle L_p \rangle = 12.4$  km  
 376 and  $\langle L_{str} \rangle = 17.6$  km while their sum is equal to the layer thickness  $Z_{layer} = 30$  km.



377  
 378 **Figure 3.** Normalized distributions of total pathlength within plasma and striations of the EMP  
 379 harmonics with the indicated frequencies for the parameters  $f_p = 5$  MHz,  $\delta = 15\%$  (a) and  $f_p = 10$   
 380 MHz,  $\delta = 50\%$  (b).

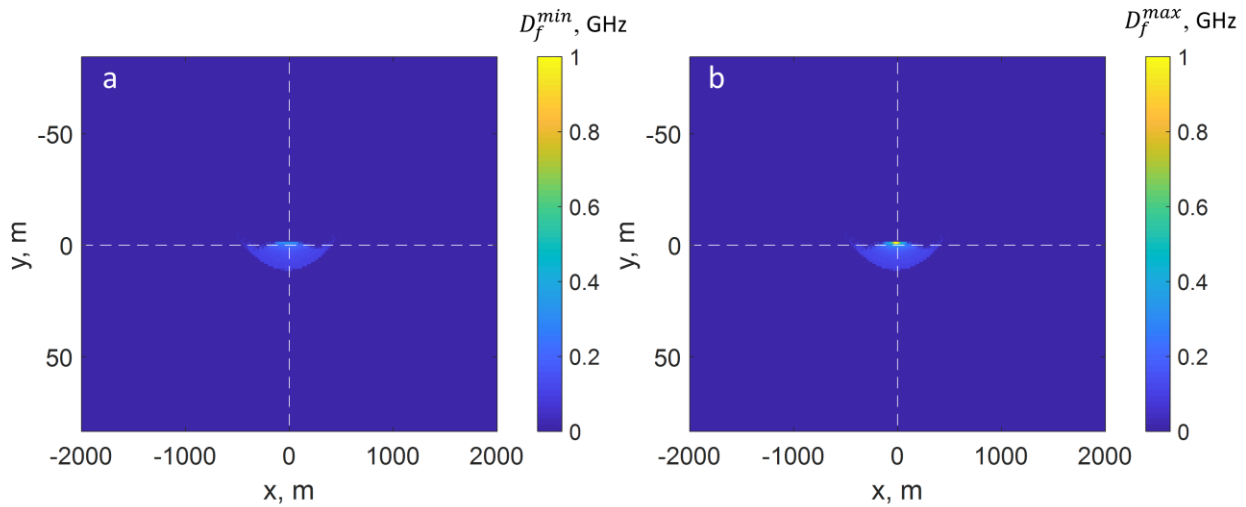


381  
 382 **Figure 4.** Average pathlength within background plasma (a) and striations (b) versus frequency  
 383 for the parameters  $f_p = 5$  MHz,  $\delta = 15\%$  (a) and  $f_p = 10$  MHz,  $\delta = 50\%$  (b).

384

385 In Fig. 5 scattering maps of minimum  $D_f^{min}$  (Fig. 5a) and maximum  $D_f^{max}$  (Fig. 3b)  
 386 frequencies from the UWB EMP discrete spectrum are shown. Spatial resolution in the maps is  
 387  $\Delta x = \Delta y = 1$  m both in the direction parallel to the projection of the cylinder axis onto the  
 388 detector plane (Y axis), and orthogonal to it (X axis). The brightest spot in both maps covers  
 389 central segment around  $(0, 0, Z_{layer})$  point of the detector plane in which all the harmonics of  
 390 the non-refracted pulse should be observed. In the case of random refraction, lower  
 391 frequencies deviate from straightforward propagation. The largest shift takes place for smallest  
 392 frequencies in the spectrum which is related to the maximum difference in the refractive  
 393 indices  $n$  and  $n_{str}$  (see Eq.(4) and Eq.(12)). The anisotropy of the frequency distribution is due  
 394 to the inclination of the irregularities at the angle of  $\alpha = 18^\circ$  with respect to vertical direction.  
 395 Non-uniform displacement is observed along Y axis, i.e., in the direction parallel to the  
 396 projection of the cylinder onto the detector plane, while in the orthogonal direction (along X)  
 397 the distribution is symmetric due to random positions of the striations relative to the initial  
 398 beam direction.

399 The  $D_f^{min}$  map (Fig. 5a) shows that all harmonics with frequencies less than 0.3 GHz  
 400 experience a shift in Y direction, and, hence, the signal in the central segment of the detector,  
 401 associated with the part of the pulse which passes through the medium without scattering, is  
 402 composed of higher harmonics. The entire scattering region for all harmonics covers the range  
 403 of  $\pm 500$  m along X-axis and less than 20 m along Y-axis. According to Fig. 5b, the highest  
 404 harmonics deviate within the limits of one segment along Y direction with size of 1 m, and  
 405 within  $\pm 20$  m along X axis.



406

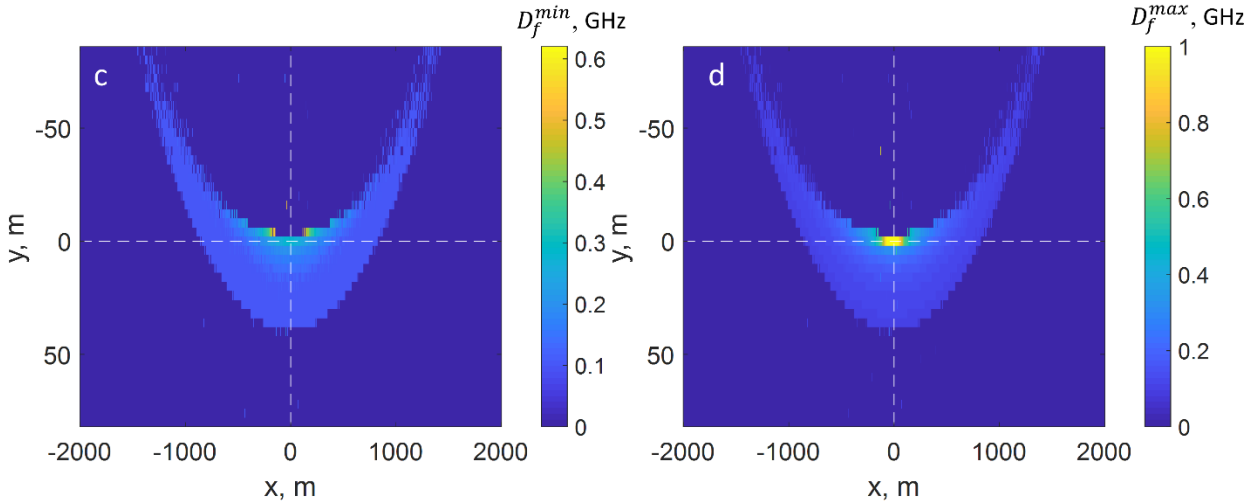


**Figure 5.** Scattering maps of minimum  $D_f^{min}$  (**a,c**) and maximum  $D_f^{max}$  (**b,d**) nonzero harmonics of EMP discrete spectrum detected after propagation within 30-km-thick plasma layer with plasma frequency of  $f_p = 5$  MHz containing Alls with variation of electron density  $\delta = 15\%$  (**a,b**) and  $\delta = 50\%$  (**c,d**).

An increase of electron density depletions depth leads to the increased scattering of EMP. Figures 3c,d show frequency scattering maps for the case of  $\delta = 50\%$  corresponding to intense irregularities. Typical size of the scattering region increases up to 120 m along Y direction, and up to  $\pm 3000$  m in X direction.  $D_f^{min}$  map (Fig.5c) shows that higher harmonics (up to 0.6 GHz) experience stronger deviation compared to the case of weaker irregularities,  $\delta = 15\%$ , (Fig. 5a) where deviation was observed for frequencies below 0.32 GHz only.

Detailed analysis of zoomed-in central parts of  $D_f^{max}$  maps (Figs.5b and 5d) shows that maximum frequencies which deviate from the central detector segment of the size  $1 \times 1 \text{ m}^2$  are below 10 GHz. This allows limiting the modeling of propagation of different harmonics by frequencies in the range of 100 MHz - 10 GHz with the step of 10 MHz. Phase delay of higher harmonics with frequencies in the range 10-50 GHz propagating in plasma with striations will can be estimated using asymptotic average path lengths  $\langle L_p \rangle$  and  $\langle L_{str} \rangle$  and asymptotic dispersion relation used in high-frequency approximation (Soldatov & Terekhin, 2016):

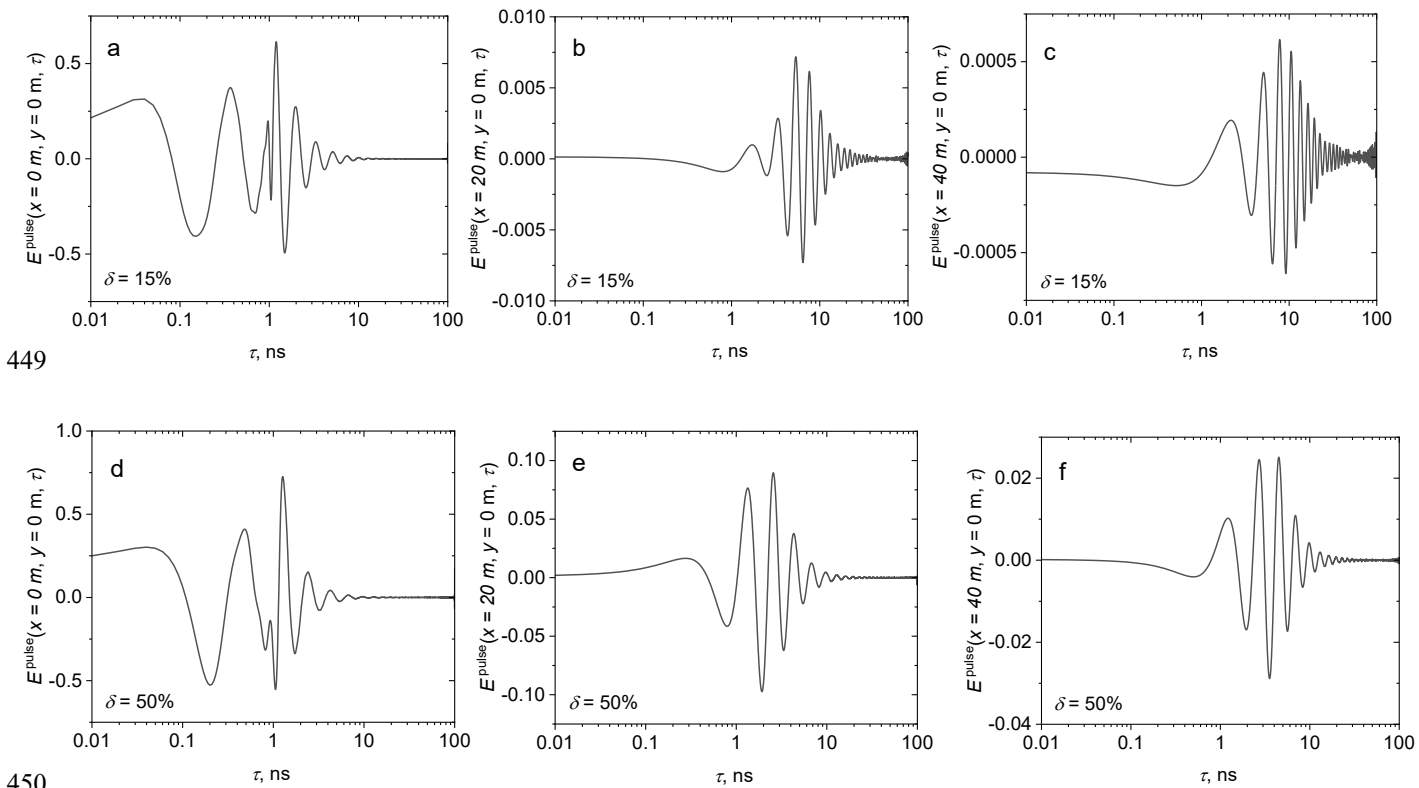
$$\phi_k^{\text{ex}} \cong \frac{2\pi f_k}{c} \left( Z_{\text{layer}} - \frac{f_p^2}{2f_k^2} (\langle L_p \rangle + (1 - \delta) \langle L_{str} \rangle) \right) \quad (19)$$

The number of harmonics in MC simulations can be thus 5 times reduced, from 5000 to less than 1000.

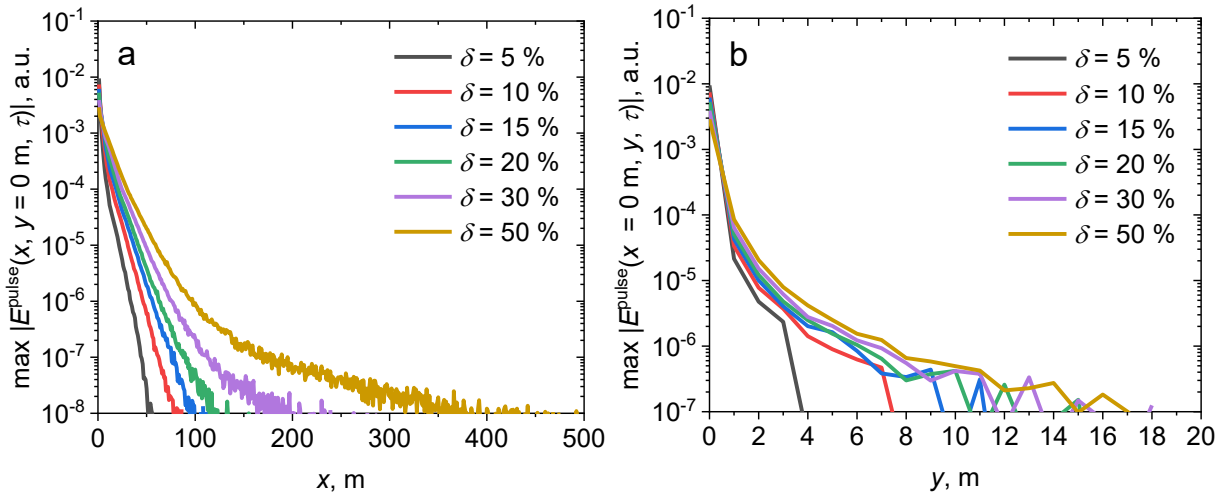
### 3.3 Scattered pulse profiles and characteristics

Figure 6 shows the waveforms of partial pulsed signals  $E^{\text{pulse}}(x, y, \tau)$  detected by different segments of the plane  $z = Z_{\text{layer}}$ . For weaker scattering with  $\delta = 15\%$  the detector segments have size  $1 \times 1 \text{ m}^2$  (Fig. 6a-c); for stronger scattering with  $\delta = 50\%$  the segment size is  $4 \times 4 \text{ m}^2$  (Fig. 6d-f). The waveforms are presented in a central segment of the detector plane

(Fig.6a, d) and size  $1 \times 1 \text{ m}^2$  (Fig. 4a) and  $4 \times 4 \text{ m}^2$  (Fig. 6d) which fully collects the pulse in the case of uniform plasma, as well as by the segments of the same size shifted along X axis at distances of 20 m (Fig. 6b, e) and 40 m (Fig. 6c, f). The waveforms of partial pulses are composed according to Eq.(15) with account for all harmonics arriving at a defined detection segment, and are plotted versus the time variable  $\tau = t - Z_{\text{layer}}/c$ . The figure demonstrates that the pulse waveform detected in the central segment and therefore composed of a large number of harmonics differs considerably from that in the shifted segments where the signal is formed by scattered harmonics at low frequencies predominantly. An attenuation of the signal amplitude as well as the delay of the pulse center of mass are observed with the increase of the transverse shift. Figure 7 presents dependences of the scattered pulse amplitudes  $\max(|E^{\text{pulse}}(x, y, \tau)|)$  versus the shift along X axis (Fig. 5a) and Y axis (Fig. 7b) for three different values of  $\delta = 15, 30, \text{ and } 50\%$ . Amplitude decays nearly exponentially in X direction for up to 100 m (Fig. 7a) with the decay rates that decrease with the increase of  $\delta$ . Slow decay at large distances is most pronounced for high  $\delta$  and is apparently related to deflection due to strong multiple refraction.

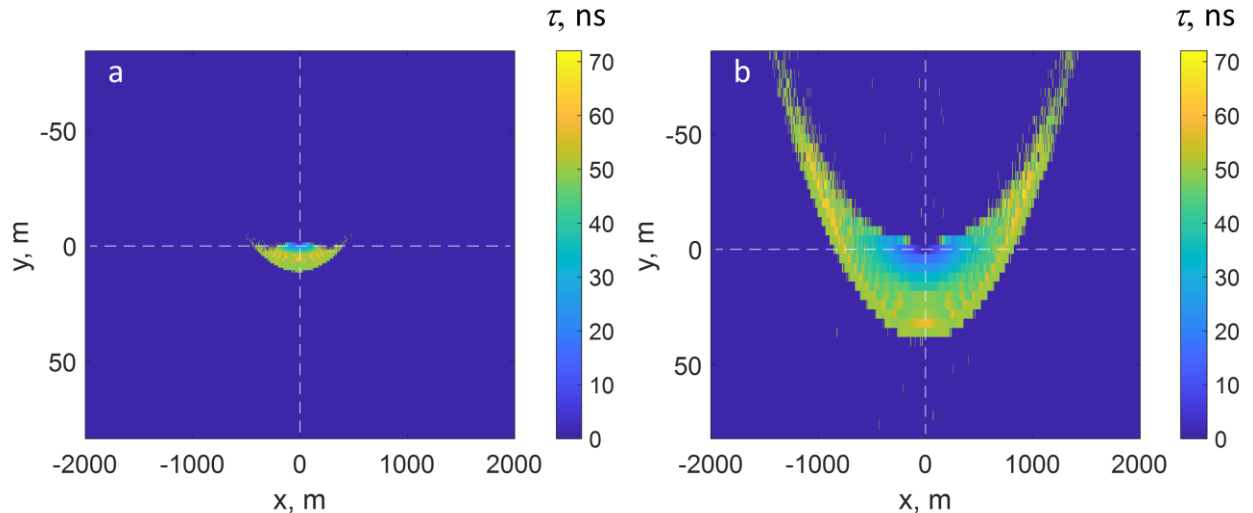


**Figure 6.** Partial pulses  $E^{\text{pulse}}(x, y, \tau)$  detected within the central segment (a,d) and segments shifted along X axis for 20 m (b,e) and 40 m (c,f) after the ray propagation in a 30-km-thick plasma layer with plasma frequency  $f_p = 5 \text{ MHz}$  in the presence of Alls with  $\delta = 15\%$  (a-c) and  $\delta = 50\%$  (d-f).



**Figure 7.** Dependence of the scattered pulse amplitude  $\max (|E^{pulse}(x, y, \tau)|)$  on transversal shift along X axis (**a**) and Y axis (**b**) after propagation in a 30-km-thick plasma layer with plasma frequency  $f_p = 5$  MHz in the presence of AIIs for various values of electron density depletion  $\delta$ .

Study of average delays of the detected partial pulses is of particular interest. In Fig. 6 maps of average delay of partial pulsed signals  $E^{pulse}(x, y, \tau)$  calculated by Eq.(5) are presented for the cases of  $\delta = 15\%$  (Fig. 8a) and  $\delta = 50\%$  (Fig. 8b). Note that in the central part of the detection plane the case of  $\delta = 15\%$  (Fig. 8a) is characterized by larger delay values compared to the case of  $\delta = 50\%$  (Fig. 8b) for a given shift of the detection segment despite stronger scattering in the latter case with larger spreading of detected rays. It should be noted that typical delays are of few ns in the segments close to the central one, and can reach 72 ns at the periphery. A detailed interpretation of this phenomenon will be given in the next section devoted to the simulation of a plane wave propagation.



470 **Figure 8.** Delay maps of detected partial pulses after the ray propagation in a 30-km-thick  
 471 plasma layer with plasma frequency  $f_p = 5$  MHz in the presence of AlIs with values of electron  
 472 density fluctuations  $\delta = 15\%$  (**a**) and  $\delta = 50\%$  (**b**).  
 473

474       **3.4 Simulation of the propagation of a nanosecond pulse in the plane wave**  
 475       **approximation**

476       To expand the presented results on the case of plane-wave EMP propagation we employ  
 477 the approach described by Eq.(18). For each harmonic, the electric fields detected within the  
 478 whole detector plane  $z = Z_{layer}$  are summarized and then all harmonics are converted into a  
 479 pulse. This simplified approach does not account for the effect of polarization change when  
 480 calculating the net field. Such an assumption was previously made in (Soldatov & Terekhin, 2016)  
 481 in a high-frequency limit. Being convenient, it yields an approximate pulse structure with  
 482 overestimated net amplitudes of the harmonics. In our study, the influence of polarization  
 483 change at the boundaries of striations may be significant for lower frequencies. However,  
 484 preliminary analysis in the frames of geometrical optics shows that depolarization of radiation  
 485 (polarization vector rotation for linearly polarized field) due to scattering on irregularities is of  
 486 the same order as the angular spread of wave vectors  $\theta_k$  of the rays arriving to the observation  
 487 point. This statement can be easily verified by considering the incidence of a beam on a flat  
 488 boundary of two isotropic media. The greatest angle of rotation of the electric field intensity  
 489 vector will be observed in the case of a TM wave, and it will be equal to the angle of rotation of  
 490 the wave vector. In the case of a TE wave, the electric field vector will not rotate at all. The  
 491 magnitude  $\theta_k$ , in its turn, can be evaluated from scattering maps (Fig.5) as  $\Omega_k \approx 0.05 - 0.1$  for  
 492 lower harmonics. Therefore, the effect of polarization change can be omitted at the current step,  
 493 while the results obtained under the stated assumption can be considered as a reference for  
 494 future detailed findings.

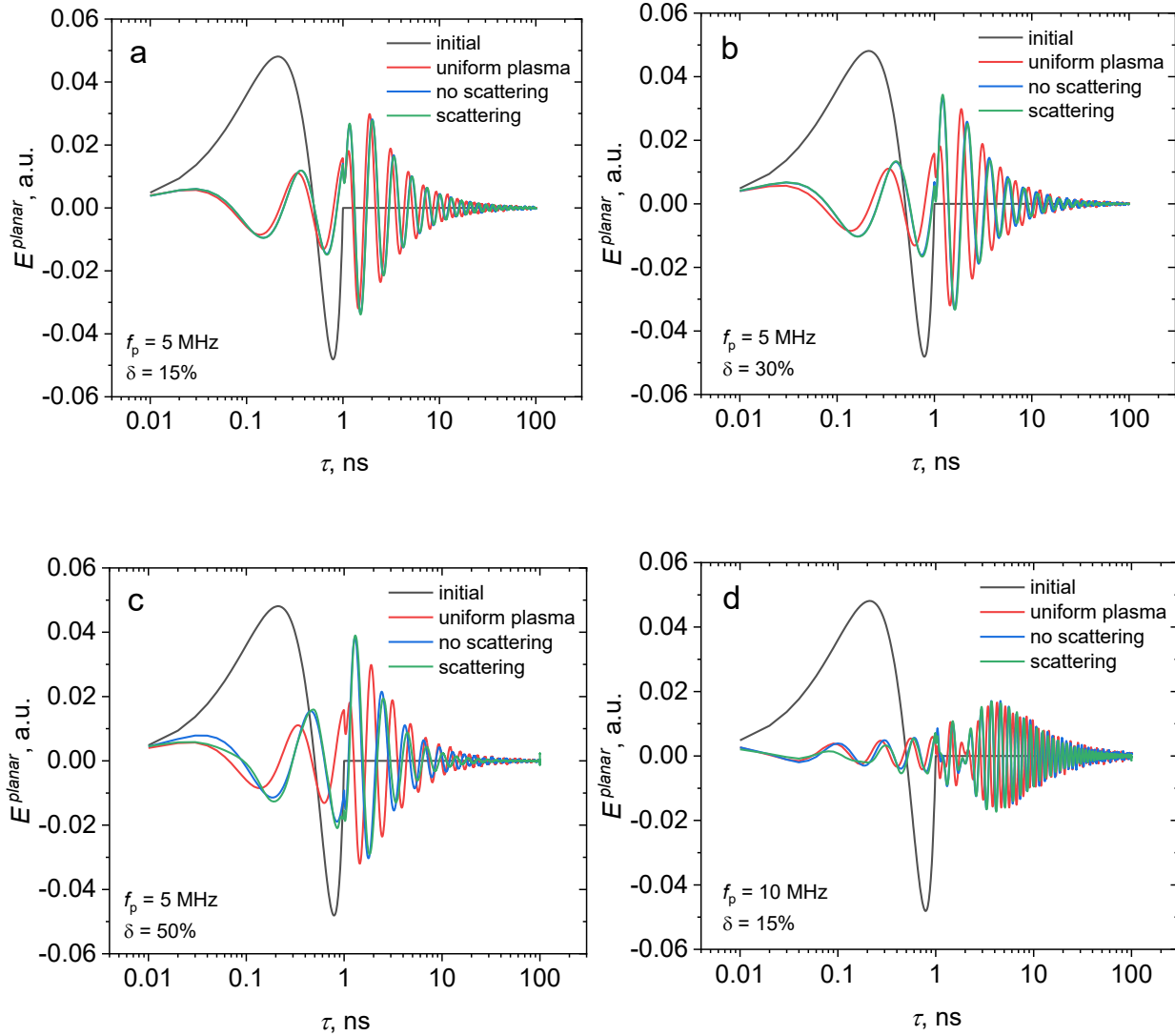
495       To demonstrate the effect of random striations **on the pulse waveform, we compared two**  
 496 **models of electron density distribution with depletion**. First model is attributed as “no scattering”  
 497 where plasma is considered as a uniform medium with an effective refractive index:

498       
$$n_{eff}(f) = \frac{\langle L_p \rangle n(f) + \langle L_{str} \rangle n_{str}(f)}{Z_{layer}} = \frac{1.24n(f) + 1.76n_{str}(f)}{3} \quad (20)$$

499       Propagation of all the harmonics in such medium is considered straight-forward with the  
 500 phase shift calculated in accordance with Eq. 15. Another model is attributed as “scattering”, and  
 501 describes the pulse propagation in plasma with cylindrical irregularities simulated by Monte Carlo  
 502 technique in accordance with Section 2.2.4.

503       The results of modeling the pulse transformation in the plane wave approximation are  
 504 presented in Fig. 9a-c for background plasma frequency  $f_p = 5$  MHz and different values of  $\delta$ . For  
 505 reference, the waveforms of the EMP propagating in uniform plasma (attributed as “uniform  
 506 plasma”) are shown. The presence of irregularities leads to the distortion of the EMP waveform  
 507 which becomes stronger with the increase of  $\delta$ . It is worth noting that the pulse waveforms in  
 508 uniform plasma differ from those in plasma with density distortions both for “no scattering” and

509 scattering" cases. The difference between the latter two cases also grows with the increase of  $\delta$   
 510 value, which is most clearly seen from Fig. 9c for  $\delta = 50\%$ .

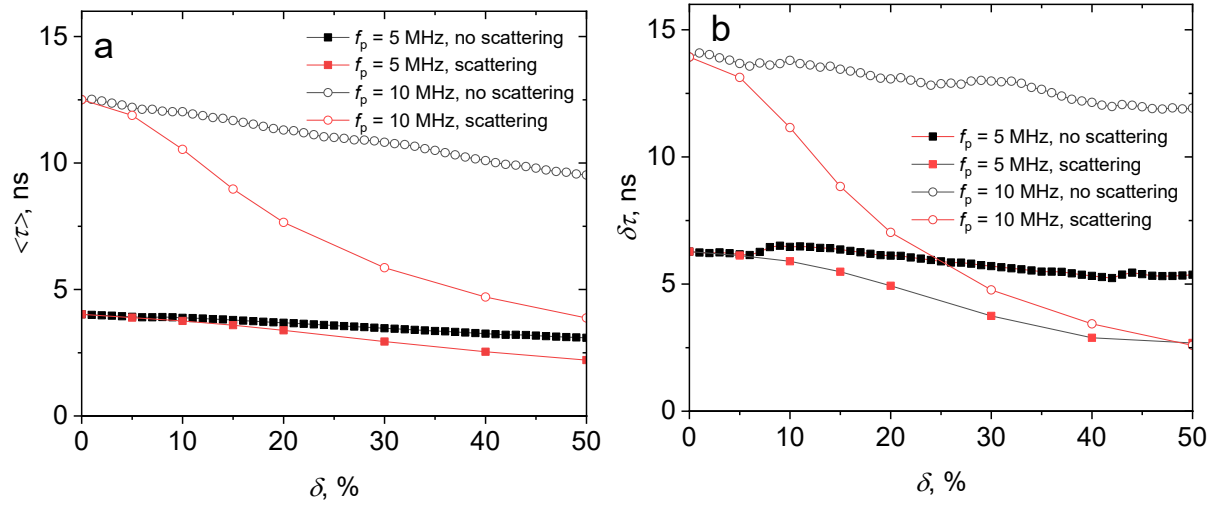


511  
 512  
 513 **Figure 9.** Waveforms of a plane wave EMP  $E^{planar}(\tau)$  after propagation in a 30-km-thick  
 514 plasma layer with background plasma frequency  $f_p = 5$  MHz for uniform plasma ("uniform  
 515 plasma"), in a medium with effective refractive index depending on electron density  
 516 fluctuations ("no scattering"), and in plasma with Alls ("scattering") for electron density  
 517 fluctuations  $\delta = 15\%$  (a),  $30\%$  (b),  $50\%$  (c), and  $\delta = 15\%$  with  $f_p = 10$  MHz (d). Initial EMP  
 518 waveform is given as a reference.

519 Figure 9d shows the results of the EMP waveform simulations for the case of high background  
 520 plasma frequency  $f_p = 10$  MHz when the refractive index dispersion is more pronounced. This  
 521 case is manifested by larger overall delays of the pulse body compared to the case of  $f_p = 5$   
 522 MHz. As it seen from comparison of the EMP waveforms in Fig.9a and Fig.9d for the same  $\delta$  but

523 different  $f_p$  values, dispersion has greater impact on the pulse shape compared to scattering  
524 effects.

525 The results of calculating the delays of the EMP center of mass by Eq.(5) are presented  
526 in Fig. 10a. Starting point of the plot is a relative delay for a pulse in uniform plasma given as a  
527 reference and indicated as “ $\delta = 0$ ”. The figure shows data for both models of density  
528 distributions (“no scattering” and “scattering” cases). In “no scattering” model, a delay of the  
529 EMP center of mass decreases with the increase of  $\delta$ , which is explained by the fact that  
530 refractive index  $n_{str}$  tends to 1 with the growth of  $\delta$ . As a result, average refractive index of the  
531 medium also becomes closer to 1 resulting in smaller effect of dispersion. What is worth noting  
532 is that the presence of scattering additionally reduces the EMP delay. This is expectable for a  
533 plasma-type medium with a refractive index below unity since larger propagation paths of  
534 scattered waves give an additional phase delay. As a result, larger propagation paths partly  
535 compensate the dispersion. This effect is especially pronounced for smaller frequencies, for  
536 which the refractive index  $n$  is smaller, however, scattering is also stronger. Moreover,  
537 scattering seems to play a more significant role in dispersion compensation for larger  $\delta$  as  
538 compared to “no scattering” case. The effect of scattering can also be illustrated by the delay  
539 maps (Fig. 8) which show angular spreading due to scattering. Curves for  $f_p = 5$  MHz and  $f_p = 10$   
540 MHz demonstrate similar systematic decrease of  $\langle \tau \rangle$  in the presence of irregularities compared  
541 to the case of EMP propagation in a uniform plasma with effective refractive index. For higher  
542 value of  $f_p$  a decrease in  $\langle \tau \rangle$  is more apparent.



543  
544

545 Fig. 10. Center of mass delay with respect to EMP propagation in free space (a) and pulse width  
546 of the pulsed plane wave (b) scattered in a 30-km-thick plasma layer with background plasma  
547 frequencies  $f_p = 5$  and 10 MHz in the presence of Alls with different values of  $\delta$ : cases of  
548 uniform plasma with effective refractive index (no scattering) and plasma with random  
549 cylindrical irregularities (scattering).

550

551 Dependences of the pulse width  $\delta\tau$  versus the value of  $\delta$  calculated by Eq.(6) are shown  
552 in Fig. 10b for both low and high plasma frequencies and demonstrate trends similar to those  
553 observed for  $\langle\tau\rangle$ . This figure also confirms that the presence of the refractive index irregularities  
554 can partly compensate dispersion effects and diminish pulse widening. As density depletions  
555 become deeper with the growth of  $\delta$ , scattering plays more significant role in compensation of  
556 EMP broadening due to the dispersion.

557 **4 Conclusions**

558 In this study, a methodology based on the Monte Carlo technique was developed for  
559 modeling the linear propagation of a nanosecond electromagnetic pulse (EMP) in ionospheric  
560 plasma in the presence of field-aligned depleted density irregularities, which are similar to well-  
561 known striations stimulated by HF heating experiments. By employing individual ray tracing  
562 approach, this technique allowed to analyze the effect of scattering by the irregularities on  
563 lower and higher frequency harmonics of the EMP for different electron densities  
564 corresponding to typical plasma frequencies from 5 MHz to 10 MHz. Due to the specific  
565 orientation of the irregularities the scattering is anisotropic and is elongated in the direction  
566 transversal to irregularities axis projection on the lower boundary of the layer with density  
567 irregularities. The harmonics below 0.3 GHz deviate from the initial direction for more than 1 m  
568 within a 30-km path, while harmonics above 10 GHz experience almost no deviation. Simulation  
569 of a plane wave propagation demonstrated two competing phenomena affecting the structure  
570 of the outcoming EMP. On the one hand, the scattering leads to energy loss in the  
571 straightforward pulse. On the other hand, average refractive index of the medium with the  
572 irregularities increases with respect to that of basic plasma leading to partial compensation of  
573 dispersion. The pulse delay and its width decrease with the increase of the electron density  
574 variation within irregularity indicating stronger role of the former phenomenon.

575 In general, field-aligned density depletions from 10% (a realistic estimate) to 50% (an  
576 overestimate) from the background value and a diameter of about 10 m do not have a  
577 significant effect on the EMP shape, which is distorted to a much greater extent due to  
578 frequency dispersion. Of course, this result requires clarification in further studies – both in  
579 terms of taking into account the effects of radiation depolarization on irregularities, and in  
580 terms of taking into account the finite radius of curvature of EMP wave front. However, at this  
581 stage it is clear that in the approximation of a plane wave of small amplitude propagating in a  
582 cold collisionless plasma, one should not expect a significant influence of scattering effects on  
583 the amplitude-temporal and spectral characteristics of EMP in the frequency band of about 1  
584 GHz and above.

585

586 **Acknowledgments**

587 The work is supported by Russian Science Foundation, project No. 24-12-00459.

588 **Data Availability Statement**

589 The simulations data are available at <https://doi.org/10.5281/zenodo.16687403>.  
 590

591 **References**

- 592 Agee, F. J., Baum, C. E., Prather, W. D., Lehr, J. M., O'Loughlin, J. P., Burger, J. W., . . . Hull, J. P. (1998). Ultra-  
 593 wideband transmitter research. *IEEE Transactions on Plasma Science*, 26(3), 860-873.
- 594 AOL, S., Buchert, S., & Jurua, E. (2020). Ionospheric irregularities and scintillations: a direct comparison of in situ  
 595 density observations with ground-based L-band receivers. *Earth, Planets and Space*, 72(1), 164.
- 596 Arnush, D. (1975). Electromagnetic pulse (EMP) propagation through an absorptive and dispersive medium. *IEEE  
 597 Transactions on Antennas and Propagation*, 23(5), 623-626.
- 598 Baum, C. E. (1992). From the electromagnetic pulse to high-power electromagnetics. *Proceedings of the IEEE*,  
 599 80(6), 789-817. doi:10.1109/5.149443
- 600 Carrano, C. S., Groves, K. M., Caton, R. G., Rino, C. L., & Straus, P. R. (2011). Multiple phase screen modeling of  
 601 ionospheric scintillation along radio occultation raypaths. *Radio Science*, 46(06), 1-14.
- 602 Cartwright, N., & Ougstun, K. (2009). Ultrawideband pulse propagation through a homogeneous, isotropic, lossy  
 603 plasma. *Radio Science*, 44(04), 1-11.
- 604 Deshpande, K., Bust, G., Clauer, C., Rino, C., & Carrano, C. (2014). Satellite-beacon Ionospheric-scintillation  
 605 Global Model of the upper Atmosphere (SIGMA) I: High-latitude sensitivity study of the model  
 606 parameters. *Journal of Geophysical Research: Space Physics*, 119(5), 4026-4043.
- 607 Dhillon, R., & Robinson, T. (2005). *Observations of time dependence and aspect sensitivity of regions of enhanced  
 608 UHF backscatter associated with RF heating*. Paper presented at the Annales Geophysicae.
- 609 Dvorak, S. L., Ziolkowski, R. W., & Dudley, D. G. (1997). Ultra-wideband electromagnetic pulse propagation in a  
 610 homogeneous, cold plasma. *Radio Science*, 32(1), 239-250.
- 611 Erukhimov, L., Metelev, S., & Razumov, D. (1988). Diagnostics of ionospheric inhomogeneities with the aid of  
 612 artificial radio emission. *Radiophysics and Quantum Electronics*, 31(11), 928-934.
- 613 Erukhimov, L. M., & Mityakov, N. A. (1989). Modification of the ionosphere as a method of its diagnostics In C. H.  
 614 Liu (Ed.), *World Ionosphere-Thermosphere Study. WITS handbook* (Vol. 2, pp. 267-284). Washington,  
 615 D.C. : National Science Foundation.
- 616 Es'kin, V. A., Korobkov, S. V., Gushchin, M. E., & Kudrin, A. V. (2023). Propagation of an ultrawideband  
 617 electromagnetic pulse along a plasma-filled coaxial line. *IEEE Transactions on Plasma Science*, 51(2),  
 618 374-380.
- 619 Fialer, P. (1974). Field-aligned scattering from a heated region of the ionosphere—Observations at HF and VHF.  
 620 *Radio Science*, 9(11), 923-940.
- 621 Franz, T., Kelley, M., & Gurevich, A. (1999). Radar backscattering from artificial field-aligned irregularities. *Radio  
 622 Science*, 34(2), 465-475.
- 623 Frolov, V., Erukhimov, L., Metelev, S., & Sergeev, E. (1997). Temporal behaviour of artificial small-scale  
 624 ionospheric irregularities: Review of experimental results. *Journal of atmospheric and solar-terrestrial  
 625 physics*, 59(18), 2317-2333.
- 626 Galiègue, H., Féral, L., & Fabbro, V. (2017). Validity of 2-D electromagnetic approaches to estimate log-amplitude  
 627 and phase variances due to 3-D ionospheric irregularities. *Journal of Geophysical Research: Space Physics*,  
 628 122(1), 1410-1427.
- 629 Golubev, A. I., Sysoeva, T. G., Terekhin, V. A., Tikhonchuk, V. T., & Altgilber, L. (2000). Kinetic model of the  
 630 propagation of intense subnanosecond electromagnetic pulse through the lower atmosphere. *IEEE  
 631 Transactions on Plasma Science*, 28(1), 303-311.
- 632 Goykhman, M., Gromov, A., Gundorin, V., Gushchin, M., Zudin, I. Y., Kornishin, S. Y., . . . Loskutov, K. (2022).  
 633 *Concept and practical implementation of a gigantic plasma-filled coaxial line for simulation of the  
 634 interaction of electromagnetic pulses with a partially ionized gas medium*. Paper presented at the Doklady  
 635 Physics.
- 636 Grach, S. M., Sergeev, E. N., Mishin, E. V., & Shindin, A. V. (2016) Dynamic properties of ionospheric plasma  
 637 turbulence driven by high-power high-frequency radiowaves. *Phys. Usp.*, 59(11), 1091-1128.  
 638 doi:10.3367/UFNe.2016.07.037868

- 639 Hong, J., Chung, J. K., Kim, Y. H., Park, J., Kwon, H. J., Kim, J. H., . . . Kwak, Y. S. (2020). Characteristics of  
 640 ionospheric irregularities using GNSS scintillation indices measured at Jang Bogo Station, Antarctica  
 641 (74.62 S, 164.22 E). *Space Weather*, 18(10), e2020SW002536.
- 642 Hunsucker, R. D., & Hargreaves, J. K. (2007). *The high-latitude ionosphere and its effects on radio propagation*:  
 643 Cambridge University Press.
- 644 Kelley, M., Arce, T., Salowey, J., Sulzer, M., Armstrong, W., Carter, M., & Duncan, L. (1995). Density depletions  
 645 at the 10-m scale induced by the Arecibo heater. *Journal of Geophysical Research: Space Physics*,  
 646 100(A9), 17367-17376.
- 647 Kim, D., Yoon, M., Lee, J., Pullen, S., & Weed, D. (2017). *Monte Carlo simulation for impact of anomalous  
 648 ionospheric gradient on GAST-D GBAS*. Paper presented at the Proceedings of the ION 2017 Pacific PNT  
 649 Meeting.
- 650 Kirillin, M. Y., Farhat, G., Sergeeva, E. A., Kolios, M. C., & Vitkin, A. (2014). Speckle statistics in OCT images:  
 651 Monte Carlo simulations and experimental studies. *Optics letters*, 39(12), 3472-3475.
- 652 Knepp, D. L. (2005). Multiple phase-screen calculation of the temporal behavior of stochastic waves. *Proceedings  
 653 of the IEEE*, 71(6), 722-737.
- 654 Leathers, R. A., Downes, T. V., Davis, C. O., & Mobley, C. D. (2004). Monte Carlo radiative transfer simulations  
 655 for ocean optics: a practical guide. *Memorandum report A*, 426624(1).
- 656 Luchinin, A., & Kirillin, M. Y. (2017). Structure of a modulated narrow light beam in seawater: Monte Carlo  
 657 simulation. *Izvestiya, Atmospheric and Oceanic Physics*, 53(2), 242-249.
- 658 Luchinin, A. G., Dolin, L. S., & Kirillin, M. Y. (2019). Time delay and width variation caused by temporal  
 659 dispersion of a complex modulated signal in underwater lidar. *Applied Optics*, 58(18), 5074-5081.
- 660 Luchinin, A. G., & Kirillin, M. Y. (2021). Angular distribution of photon density waves radiance in media with  
 661 different scattering anisotropy. *Applied Optics*, 60(31), 9858-9865.
- 662 Luchinin, A. G., Kirillin, M. Y., & Dolin, L. S. (2024). Evolution of temporal and frequency characteristics of  
 663 spherical photon density waves in scattering media. *Journal of Quantitative Spectroscopy and Radiative  
 664 Transfer*, 312, 108799.
- 665 Mahmoudian, A., Scales, W., Taylor, S., Morton, Y., Bernhardt, P., Briczinski, S., & Ghader, S. (2018). Artificial  
 666 ionospheric gps phase scintillation excited during high-power radiowave modulation of the ionosphere.  
 667 *Radio Science*, 53(6), 775-789.
- 668 Marchuk, G. I., Mikhailov, G. A., Nazareliev, M., Darbinjan, R. A., Kargin, B. A., & Elepov, B. S. (2013). *The  
 669 Monte Carlo methods in atmospheric optics* (Vol. 12): Springer.
- 670 Milikh, G., Gurevich, A., Zybin, K., & Secan, J. (2008). Perturbations of GPS signals by the ionospheric  
 671 irregularities generated due to HF-heating at triple of electron gyrofrequency. *Geophysical Research  
 672 Letters*, 35(22).
- 673 Mountcastle, P. D., & Martin, M. D. (2002). Monte Carlo simulation of ionospheric scintillation. *Proceedings of the  
 674 2002 IEEE Radar Conference* (IEEE Cat. No. 02CH37322), 350 – 355.
- 675 Mrak, S., Coster, A. J., Groves, K., & Nikoukar, R. (2023). Ground-based infrastructure for monitoring and  
 676 characterizing intermediate-scale ionospheric irregularities at mid-latitudes. *Frontiers in Astronomy and  
 677 Space Sciences*, 10, 1091340.
- 678 Najmi, A., Milikh, G., Secan, J., Chiang, K., Psiaki, M., Bernhardt, P., . . . Papadopoulos, K. (2014). Generation and  
 679 detection of super small striations by F region HF heating. *Journal of Geophysical Research: Space  
 680 Physics*, 119(7), 6000-6011.
- 681 Nekoogar, F. (2011). *Ultra-Wideband Communications: Fundamentals and Applications* Fundamentals and  
 682 Applications: Prentice Hall Press.
- 683 Perkins, F. (1975). Ionospheric irregularities. *Reviews of Geophysics*, 13(3), 884-884.
- 684 Robinson, T. (2002). Effects of multiple scatter on the propagation and absorption of electromagnetic waves in a  
 685 field-aligned-striated cold magneto-plasma: implications for ionospheric modification experiments.  
 686 *Annales Geophysicae*, 20, 41-55.
- 687 Sato, H., Rietveld, M. T., & Jakowski, N. (2021). GLONASS observation of artificial field-aligned plasma  
 688 irregularities near magnetic zenith during EISCAT HF experiment. *Geophysical Research Letters*, 48(4),  
 689 e2020GL091673.
- 690 Schlegel, K. (1973). Monte Carlo simulation of a model ionosphere—II. Energy flow and energy dissipation.  
 691 *Journal of Atmospheric and Terrestrial Physics*, 35(3), 415-424.
- 692 Sergeeva, E. A., Kirillin, M. Y., & Priezzhev, A. V. e. (2006). Propagation of a femtosecond pulse in a scattering  
 693 medium: theoretical analysis and numerical simulation. *Quantum Electronics*, 36(11), 1023.

- 694 Soldatov, A., & Terekhin, V. (2016). Propagation of an ultrawideband electromagnetic signal in ionospheric plasma.  
695     *Plasma Physics Reports*, 42(10), 970-977.
- 696 Streltsov, A., Berthelier, J.-J., Chernyshov, A., Frolov, V., Honary, F., Kosch, M., . . . Rietveld, M. (2018). Past,  
697     present and future of active radio frequency experiments in space. *Space Science Reviews*, 214(8), 118.
- 698 Wernik, A., Secan, J., & Fremouw, E. (2003). Ionospheric irregularities and scintillation. *Advances in Space  
699     Research*, 31(4), 971-981.
- 700 Xiong, G., Xue, P., Wu, J., Miao, Q., Wang, R., & Ji, L. (2005). Particle-fixed Monte Carlo model for optical  
701     coherence tomography. *Optics express*, 13(6), 2182-2195.
- 702 Yan, S., & Fang, Q. (2020). Hybrid mesh and voxel based Monte Carlo algorithm for accurate and efficient photon  
703     transport modeling in complex bio-tissues. *Biomedical Optics Express*, 11(11), 6262-6270.
- 704 Zhang, T., Li, Z., Duan, C., Wang, L., Wei, Y., Li, K., . . . Cao, B. (2024). Design of a High-Power Nanosecond  
705     Electromagnetic Pulse Radiation System for Verifying Spaceborne Detectors. *Sensors (Basel, Switzerland)*,  
706     24(19), 6406.
- 707 Zudin, I., Gushchin, M., Korobkov, S., Strikovskiy, A., Katkov, A., Kochedykov, V., & Petrova, I. (2024).  
708     Transformation of the Shape and Spectrum of an Ultrawideband Electromagnetic Pulse in a “Gigantic”  
709     Coaxial Line Filled with Magnetized Plasma. *Applied Sciences*, 14(2), 705.
- 710

711